Available online at www.sciencedirect.com
SCIENCE DIRECT®
Mechanics of Materials 35 (2003) 969–986
MECHANICS OF MATERIALS
www.elsevier.com/locate/mechmat

An experimental study of the superelastic effect in a shape-memory Nitinol alloy under biaxial loading

J.M. McNaney [a,1], V. Imbeni [a], Y. Jung [b], Panayiotis Papadopoulos [b], R.O. Ritchie [a,*]

[a] Department of Materials Science and Engineering, University of California, Berkeley, CA 94720-1760, USA
[b] Department of Mechanical Engineering, University of California, Berkeley, CA 94720, USA

Received 24 May 2002; received in revised form 10 September 2002

Abstract

Constitutive laws for shape-memory alloys subjected to multiaxial loading, which are based on direct experimental observations, are generally not available in the literature. Accordingly, in the present work, tension–torsion tests are conducted on thin-walled tubes (thickness/radius ratio of 1:10) of the polycrystalline superelastic/shape-memory alloy Nitinol using various loading/unloading paths under isothermal conditions. The experimental results show significant variations in the mechanical response along the two loading axes. These are attributed to changes in the martensitic variants nucleated in response to the directionality of the applied loading, as well as to microstructural texture present in the parent material. Numerical simulations suggest that the characterization and modeling of the microstructure is of paramount importance in understanding the phenomenology of shape-memory alloys.

Keywords: Shape-memory alloys; Phase transformation; Superelasticity; NiTi; Nitinol; Constitutive behavior; Multiaxial loading

1. Introduction

Shape-memory alloys exhibit strongly non-linear thermomechanical response associated with stress- or temperature-induced transformations of their crystalline structure. These reversible transformations lead to the special properties of superelasticity and shape memory; see (Wayman and Duerig, 1990; Sun and Hwang, 1993) for a brief illustrative description of these properties. Nitinol, a nearly equiatomic NiTi alloy originally brought into practice by Buehler and Wiley (1965), is one of very few alloys that are both superelastic and biocompatible; moreover, the temperature range within which Nitinol superelasticity is exhibited includes human body temperature (Duerig et al., 2000). As a result, Nitinol is now widely used in

* Corresponding author. Tel.: +1-510-486-5798; fax: +1-510-486-4995.
E-mail address: roritchie@lbl.gov (R.O. Ritchie).
[1] Present address: Materials Science and Technology Division, Lawrence Livermore National Laboratory, University of California, Berkeley, CA 94720, USA.

0167-6636/$ - see front matter © 2002 Elsevier Ltd. All rights reserved.
doi:10.1016/S0167-6636(02)00310-1

biomedical devices such as endovascular stents, *vena cava* filters, dental files, archwires and guidewires, etc.

Both the superelasticity and shape-memory effects are induced in Nitinol by reversible, displacive, diffusionless, solid–solid phase transformations from a highly ordered austenitic (simple cubic, B2) crystal structure to a less ordered martensitic (B19′, monoclinic) structure. The stress-induced austenite-to-martensite transformation is effected by the formation of martensitic structures which correspond to system energy minimizers. Although 24 variants of the less symmetric martensitic phase can be formed by the same crystal of parent austenite, it has been experimentally observed that only a few variants are typically active and fully resolve the stress/shape change (Miyazaki et al., 1989; Gall and Sehitoglu, 1999). During the martensite-to-austenite (reverse) transformation, all variants transform back to the same parent phase.

Most of the mechanical testing on polycrystalline Nitinol found in the literature has been performed on wires and is thus one-dimensional. As a result, most phenomenological constitutive models are based on uniaxial data, oftentimes extended to three-dimensions in an ad hoc fashion. Hence, there is little confidence that three-dimensional models can accurately describe the material response under complex loading experienced in Nitinol devices. Very little information exists on the multiaxial loading/unloading of Nitinol and even less on tubes which are used as the starting material in the manufacture of critical devices such as endovascular stents; to our knowledge, only three previous studies, all on thick-walled tubing, are available (Miyazaki et al., 1989; Lim and McDowell, 1999; Helm and Haupt, 2001).

The present work focuses on the biaxial testing of thin-walled tubes chosen to minimize the gradient in the torsional strain along the radial direction. Three distinct biaxial stress-loading paths are explored under isothermal conditions. The resulting data are compared to the results obtained by numerical simulation of polycrystalline Nitinol response based on an extension to polycrystalline response and to finite deformations of a three-dimensional single-crystal model by Siredey et al. (1999).

The organization of the article is as follows: the experimental protocol and the testing setup are described in Section 2. The experimental results are documented in Section 3. These are followed by discussion and comparison to numerical simulations in Section 4 and concluding remarks in Section 5.

2. Experimental procedure

2.1. Materials

Nitinol tubing (Ti 49.2 at.%, Ni 50.8 at.%) was received from NDC (Fremont, CA), with a 4.64 mm outer diameter and 0.37 mm thickness. The tubing was cut into 75 mm long specimens and ground down along the 25 mm long center test section to an outer diameter of 4.3 mm in order to obtain an hourglass shape and minimize end-effects during testing (Fig. 1). Thus, the wall thickness in the gauge section was reduced to 0.2 mm, resulting in a thickness-to-radius ratio of approx-

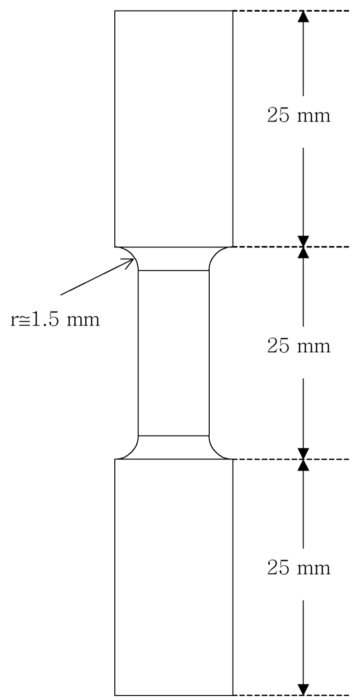

Fig. 1. Schematic illustration of the NiTi specimen (not to scale).

imately 1:10. The specimens were subsequently heat-treated at 485 °C in air for 5 min and then water-quenched to bring the austenite finish temperature slightly below room temperature. This treatment produces a complex microstructure consisting of equiaxed low-angle subgrains of approximately 1 μm in size within irregularly shaped parent grains of approximately 25 μm in size. The heat treatment also yields extremely fine Ni-rich precipitates of Ni_4Ti_3 and $Ni_{14}Ti_{11}$ within the NiTi matrix. The subgrain boundaries and the precipitates make dislocation movement difficult; thus they are important in achieving optimum superelasticity. The precipitates also play an important role in the "fine-tuning" of the transformation temperature, which is critical in achieving desired superelastic properties. Also present in the microstructure are roughly equiaxed and insoluble Ti_4Ni_2O oxide particles of a size up to approximately 1 μm.

The nature of the microstructure makes both optical and electron microscopy very difficult, producing complex and difficult to interpret images. In fact, an additional complicating factor is that the stresses due to polishing tend to produce martensite, and, even in electropolished surfaces, triaxial constraint is lost, leading to a modification of the hysteresis and thus again, martensite artifacts are observed. A full microstructural analysis is deemed to be beyond the scope of this work. For the present experiments, it is sufficient to note that optical metallography of the tubing cross section has confirmed that there are approximately 8–15 grains traversed through the wall thickness (Fig. 2).

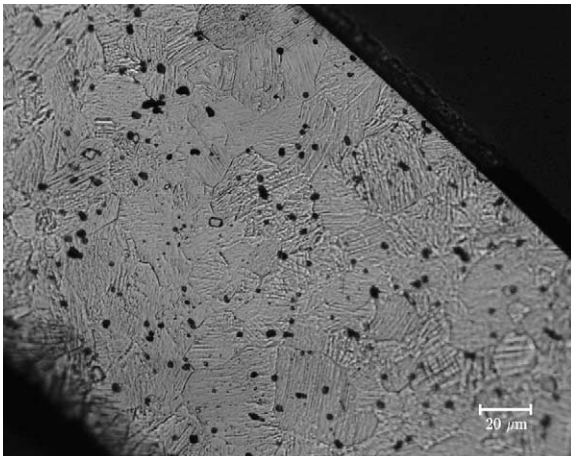

Fig. 2. Optical micrograph of the cross section of a thin-walled tubular specimen of Nitinol (the edges of the tube are visible), showing an average grain size of approximately 25 μm with fine Ni-rich precipitates (etched for 30 s in an aqueous solution of 3.2 vol.% HF and 12.1 vol.% HNO_3).

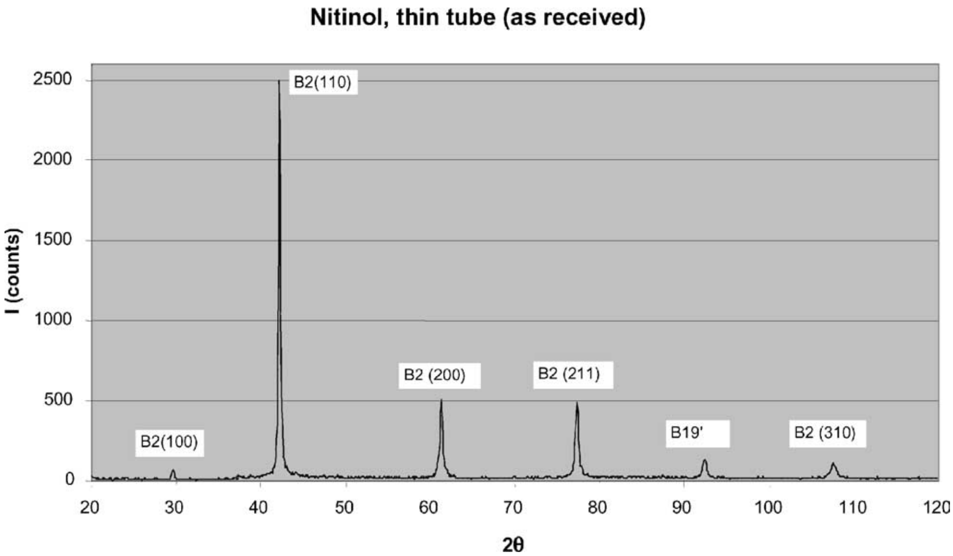

Fig. 3. X-ray diffraction analysis of the as received NiTi material showing an essentially fully austenitic structure.

The martensite/austenite transformation temperatures of the heat-treated samples were characterized by differential scanning calorimetry and were found to be $A_s = -6.36$ °C (austenite start), $A_f = 18.13$ °C (austenite finish), and $M_s = -51.55$ °C (martensite start), $M_f = -87.43$ °C (martensite finish), respectively. X-ray diffractometry conducted at the Stanford Synchrotron Radiation Laboratory was used to observe the phases present before and after the tests. A negligible amount of martensite (on the order of 1%) was detected prior to testing (Fig. 3).

2.2. Mechanical testing

The mechanical test setup is shown in Fig. 4. As the shape change during the austenite-to-martensite transformation can create slippage problems in the grips, reliable tests could not be performed with straight tubes. To circumvent these problems, two strategies were simultaneously employed. First, tubes with a gauge section of reduced diameter were used in order to minimize end-effects at the grips and to lower the stress in the gripped section, as described in Section 2.1. Second, a split-grip design was employed, as shown in Fig. 5; a

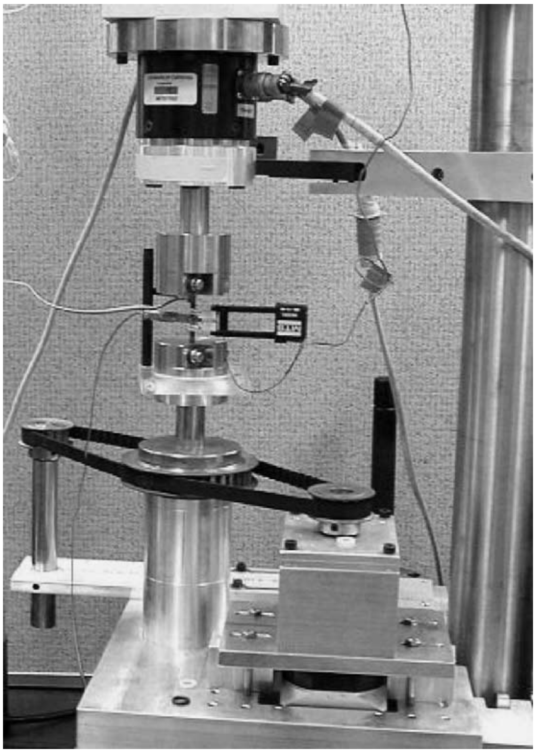

Fig. 4. General view of the experimental setup.

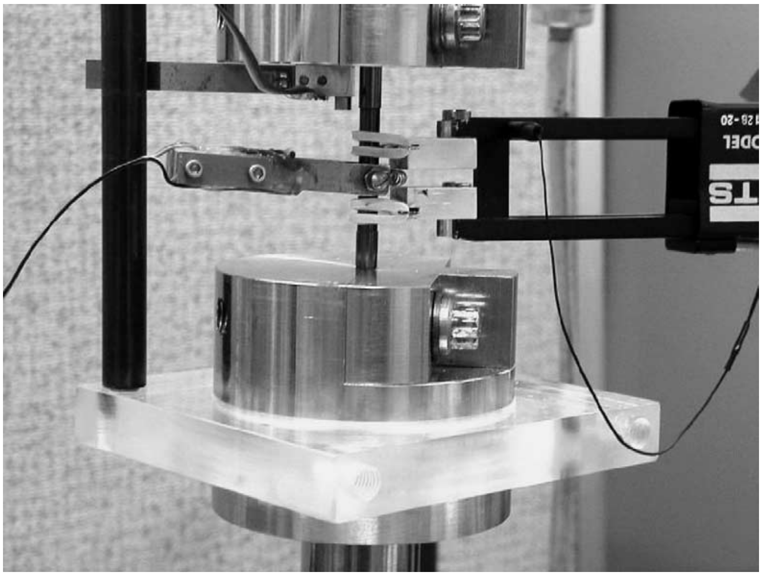

Fig. 5. Detail of the gripping configuration.

hardened steel pin was inserted into the tube throughout the grip region which allowed application of sufficient lateral gripping force to inhibit slippage during testing.

Strain rates in the range 10^{-5}–10^{-4} s^{-1} were used for both the tensile and torsional loading in order to avoid rate effects. Due to the two-dimensional nature of the loading paths, the strain rates could not be fixed for the entire test. For pure tension and pure torsion segments, the strain rate during loading/unloading was 10^{-4} s^{-1}. During mixed-mode proportional loading/unloading tests, the tensile strain rate was fixed at 10^{-4} s^{-1}, while the shearing strain rate was adjusted to maintain the prescribed loading path. For the material used in this study, preliminary uniaxial tests using slower loading rates confirmed that the range of strain rates employed did not affect the measured stress–strain response.

All testing was performed at an ambient temperature of 22 °C that was maintained to within ± 1 °C during any single test. The loading rates used in the experiments were shown to be sufficiently low to suppress significant temperature variations during testing (Lim and McDowell, 1995). Indeed, a surface-mounted resistance temperature detector used in a tensile loading test at strain rate of 5×10^{-4} s^{-1} recorded a temperature rise of less than 1.5 °C. Hence, all experiments were deemed to be taking place under essentially isothermal conditions.

Using thin-walled tubes, three measurements are necessary in order to fully characterize the strain state of the material: tensile elongation, radial elongation, and angle of twist. Tensile elongation was measured using a standard extensometer mounted over a 13 mm gauge length in the reduced section of the tube. The extensometer was attached to the specimen using elastomeric bands. Radial elongation was measured in the reduced section using a spring-loaded clip gauge outfitted with a semicircular clamping region. Attempts to mount an angular measurement device directly on the reduced section of the tube were unsuccessful due to excessive gauge slippage during the austenite-to-martensite transformation. Consequently, angular rotation of the tube was measured at the grip. The following procedure was used to determine the rotation in the reduced (gauge) section of the tube:

(i) The total angular rotation ϕ_t of the specimen was measured.
(ii) The elastic rotation ϕ_e of the thick-walled section of tubing between the gauge section and the grip was calculated based on the length of the thick-walled section and the calibrated response of a straight thick-walled tube.
(iii) The rotation of the gauge section ϕ of the tube was found by subtracting the elastic rotation of the (thick-walled) tube section from the total measured angular rotation, namely $\phi = \phi_t - \phi_e$.

It is noted that when loading in pure torsion under fixed tensile displacement, a tensile clip gauge response was presumed to be due to torsion (i.e., as the tube twists, the gauge might slip slightly). In addition, a constant value of tensile strain during pure torsional loading was assumed.

All axial and torsional loads were measured using a tension–torsion load cell (Key Transducers Inc., model 6104–10, capacity 28 Nm/4500 N for torsion–tensile, respectively).

2.3. Loading program

In order to investigate thoroughly the complex nature of the forward and reverse transformation process and its effect on the constitutive properties of polycrystalline Nitinol, three specific loading/unloading programs (referred to as Types I–III) were investigated, as outlined below:

Type I (Load in tension followed by torsion, unload in reverse order—Fig. 6(a))
1. Tensile loading to a particular strain level; hold during segments 2 and 3.
2. Torsional loading to 2% shear strain.
3. Unload shear axis to zero strain.
4. Unload tensile axis to zero strain.

Type II (Load in torsion followed by tension, unload in reverse order—Fig. 6(b))
5. Torsional loading to 2% shear strain; hold during segments 2 and 3.
6. Tensile loading to a particular strain level.

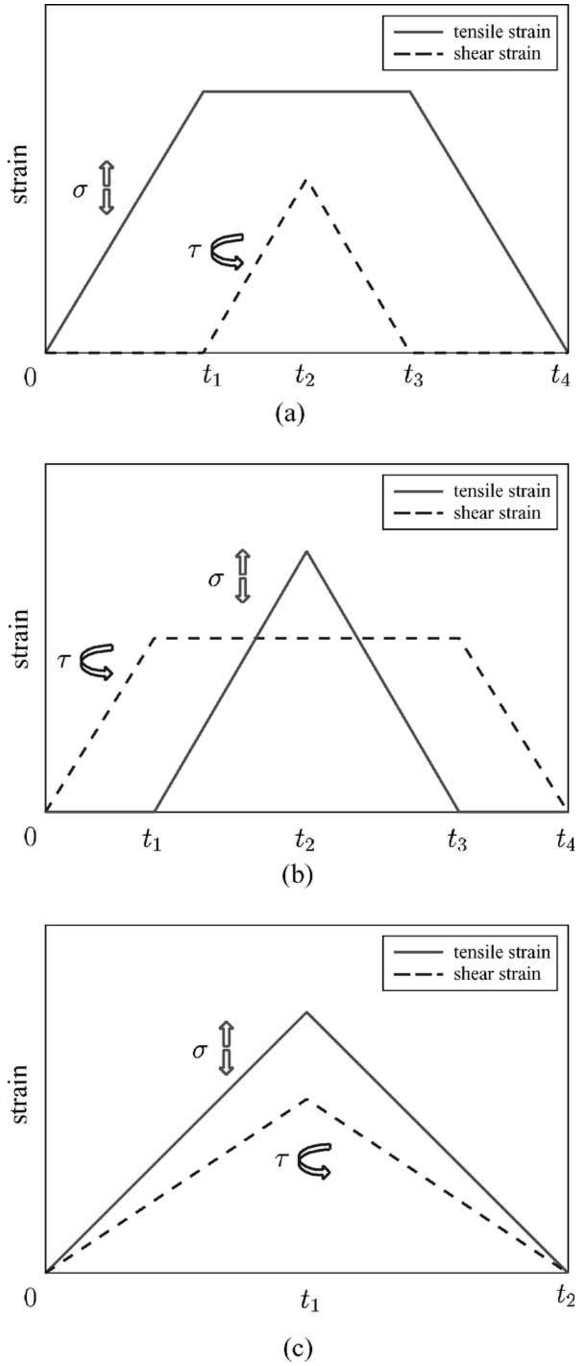

Fig. 6. Strain/time sequence for Types I–III loading. (a) Tension followed by torsion (Type I); (b) torsion followed by tension (Type II) and (c) simultaneous tension–torsion (Type III).

7. Unload tensile axis to zero strain.
8. Unload shear axis to zero strain.

Type III (Load and unload in simultaneous tension–torsion—Fig. 6(c))

9. Load simultaneously in tensile and torsional axes. Rates for each axis were independently controlled so that the end strain was reached simultaneously.
10. Unload tensile and torsional axes simultaneously to zero strain.

A series of specific loading paths were considered for Types I–III. Tensile strains ranging from 0% to 6.0% were considered. The maximum attainable shear strain was limited to 2% due to buckling of the thin-walled structure. However, given that forward transformation is initiated at approximately 1% shear strain, this limit did not substantially restrict the mapping of the loading in the shear strain dimension. A minimum of two repetitions were carried out for each loading path considered.

3. Results

Results of the experiments conducted in this study are presented in Figs. 7,9–18 as plots of equivalent true (Cauchy) stress σ_{eq} versus equivalent referential (Lagrangian) strain ε_{eq}, namely:

$$\sigma_{eq} = \sqrt{\sigma_t^2 + 3\sigma_s^2}, \quad \varepsilon_{eq} = \sqrt{\varepsilon_t^2 + \frac{4}{3}\varepsilon_s^2},$$

where σ_t and ε_t (respectively σ_s and ε_s) denote the tensile (respectively shearing) stress and strain. Within acceptable experimental error margins, the unloading of all stress–strain curves passes back through the origin in all tests; this indicates that the transformation is reversible and displays the superelastic effect independently of the loading path.

3.1. Uniaxial tension and torsion

Pure tension results are shown in Fig. 7 and reveal behavior typical of shape-memory alloys in the superelastic regime. The initial elastic response is followed by a plateau region, during which

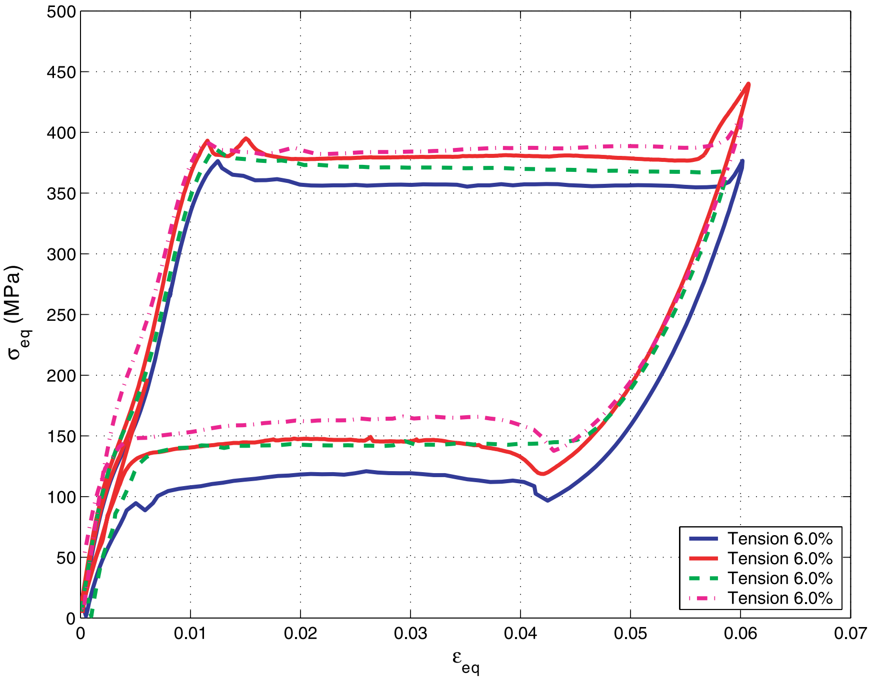

Fig. 7. Equivalent stress–strain plot showing the repeatability of four separate uniaxial tension tests up to 6% strain.

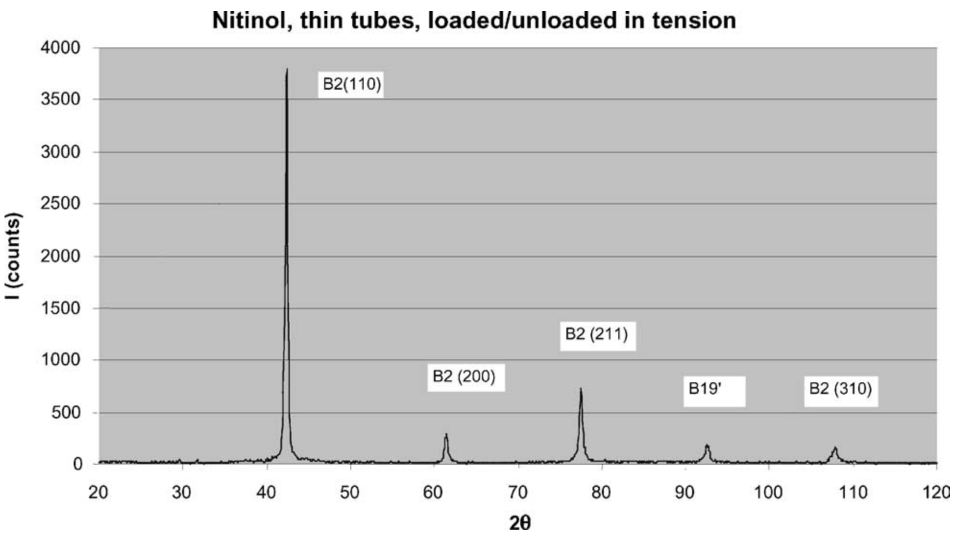

Fig. 8. X-ray diffraction analysis of NiTi material after a complete tension cycle, showing the presence of a small proportion of residual martensite.

forward transformation occurs under increasing strains. Upon completion of the transformation at approximately 5.75% strain, further loading results in elastic deformation of the fully transformed martensite matrix. Unloading of the transformed material is initially elastic, followed by a second plateau region, during which most of the reverse transformation occurs. Finally, elastic unloading of the regenerated austenite phase takes place. The repeatability of the tests appears to be adequate with the onset of the transformation varying between 1.1% and 1.2% strain and the transformation plateau stresses lying between 355 and 380 MPa. These variations may be attributed to the sensitivity of the material to small ambient temperature changes. Fig. 8 shows typical X-ray diffraction data, for a specimen that has been loaded and unloaded in tension, which reveal the presence of a small proportion of residual martensite.

Under pure torsional loading (Fig. 9), the transition from the elastic loading region to the transformation plateau region is less sharp. Notice that the lack of closure in the loading/unloading curve is due to the slippage of the axial extensometer. This conclusion is deduced by a simple comparison with the corresponding shear (as opposed to equivalent) stress–strain diagram in Fig. 10, where closure is accurately reproduced.

3.2. Tension followed by torsion (Type I)

Results of Type I loading experiments involving tension up to a maximum of 6% strain, followed by torsional loading of 2% strain and reverse-order unloading are presented in Fig. 11. Even with this relatively simple loading path, the material response is quite complex. A number of qualitative features, however, are evident. At low tensile strains (<1%), the overall behavior is similar to that of pure torsion; at higher tensile strains, a sharp increase is observed in the stress upon superposition of torsion, which is indicative of the generation of a new set of martensitic variants which are energetically preferable for torsional (rather than the tensile) deformation. In addition, the hysteresis in the torsional loading/unloading loop appears to decrease progressively with increasing applied tensile strain

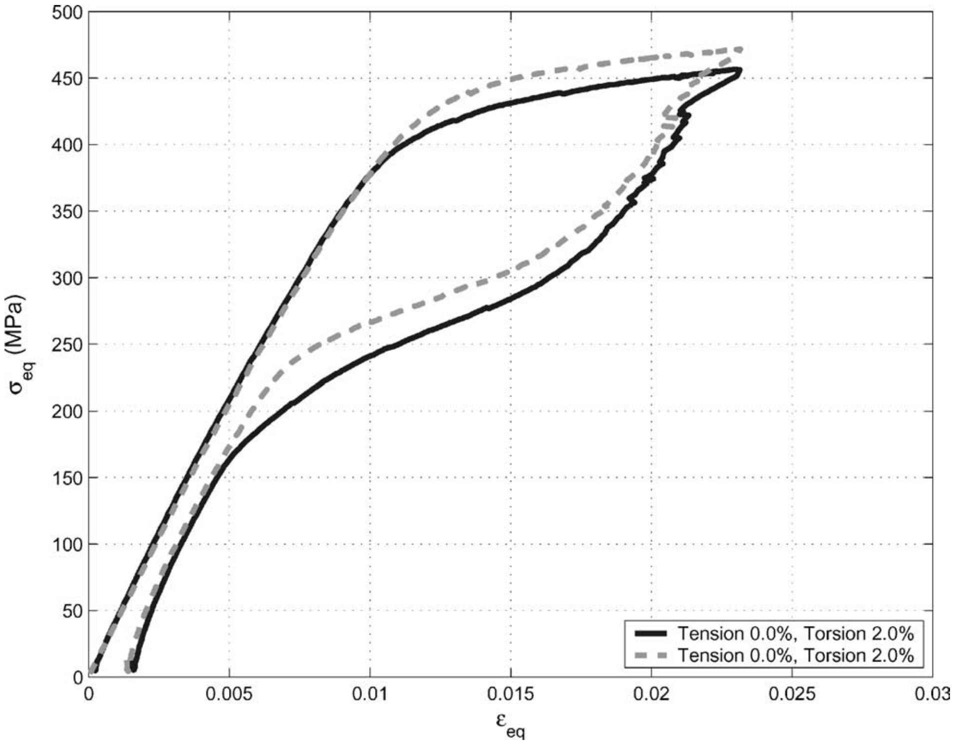

Fig. 9. Equivalent stress–strain plot showing the repeatability of two separate uniaxial torsion tests up to 2.3% equivalent strain.

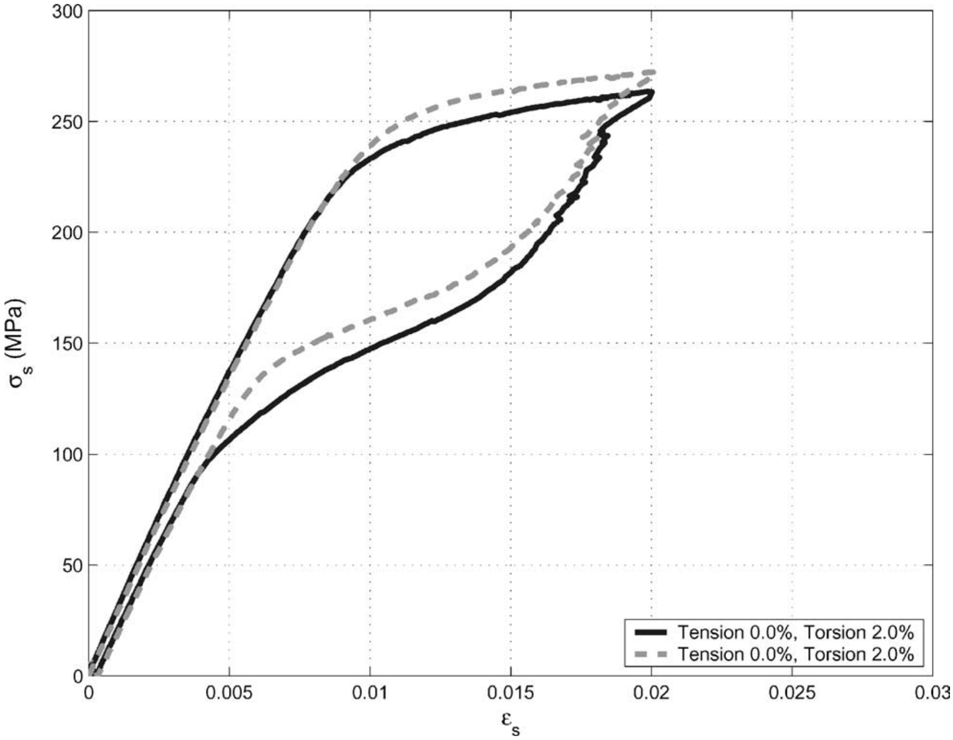

Fig. 10. Shear stress–strain plot showing the repeatability of two separate uniaxial torsion tests up to 2.0% shear strain.

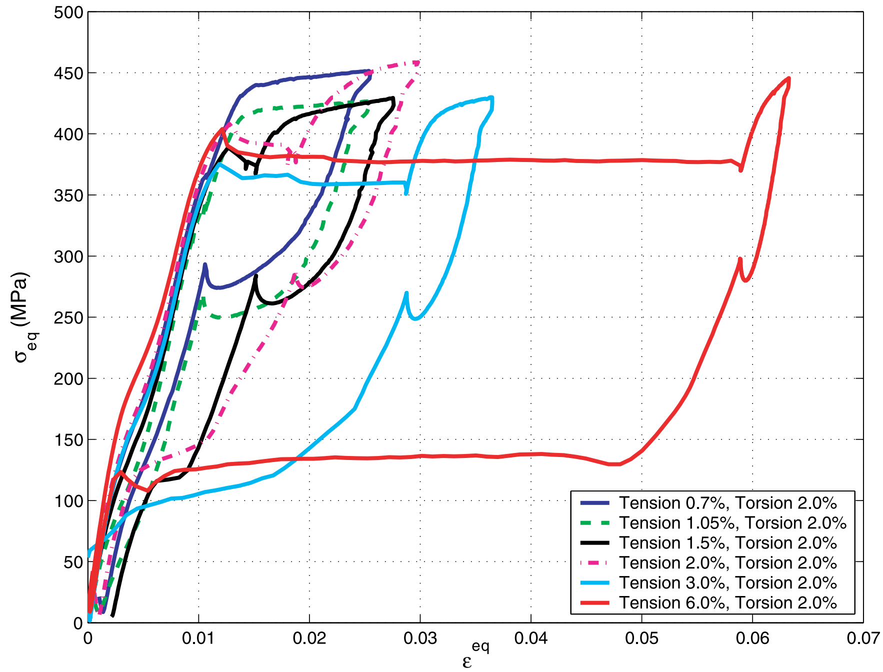

Fig. 11. Equivalent stress–strain plots in tension (0%, 0.7%, 1.10%, 1.5%, 2%, 3%, 6%), followed by torsion (2%) and reverse unloading (Type I).

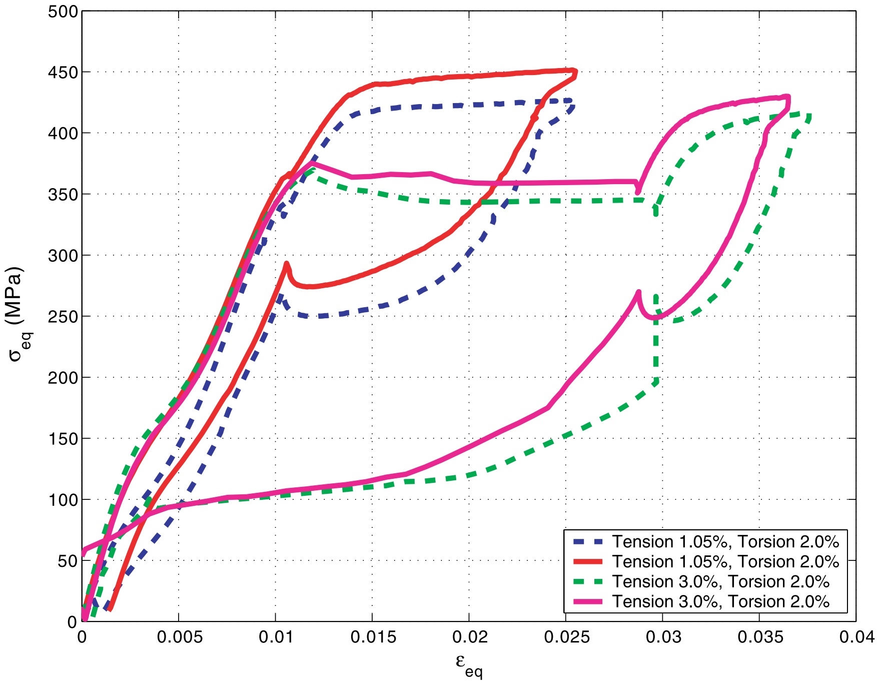

Fig. 12. Equivalent stress–strain plot showing the repeatability of tension–torsion tests at two different sets of tensile strain (1.05%, 3%) and 2% shear strain.

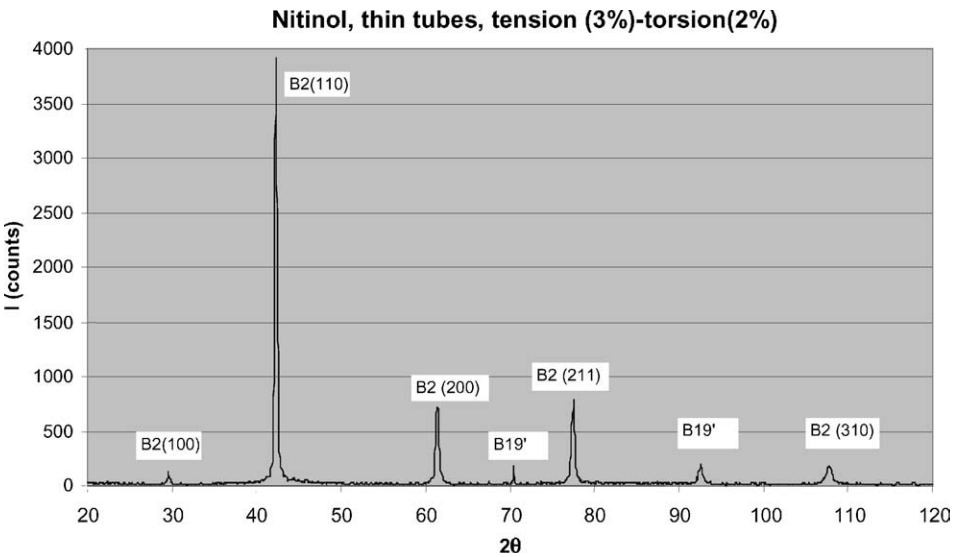

Fig. 13. X-ray diffraction analysis of NiTi material after a complete tension–torsion cycle, showing the presence of a small proportion of residual martensite.

which is consistent with the decreasing volume fraction of variants associated with torsion. At all levels of applied tensile strain, the end of the torsional unloading segment is marked by a increasing

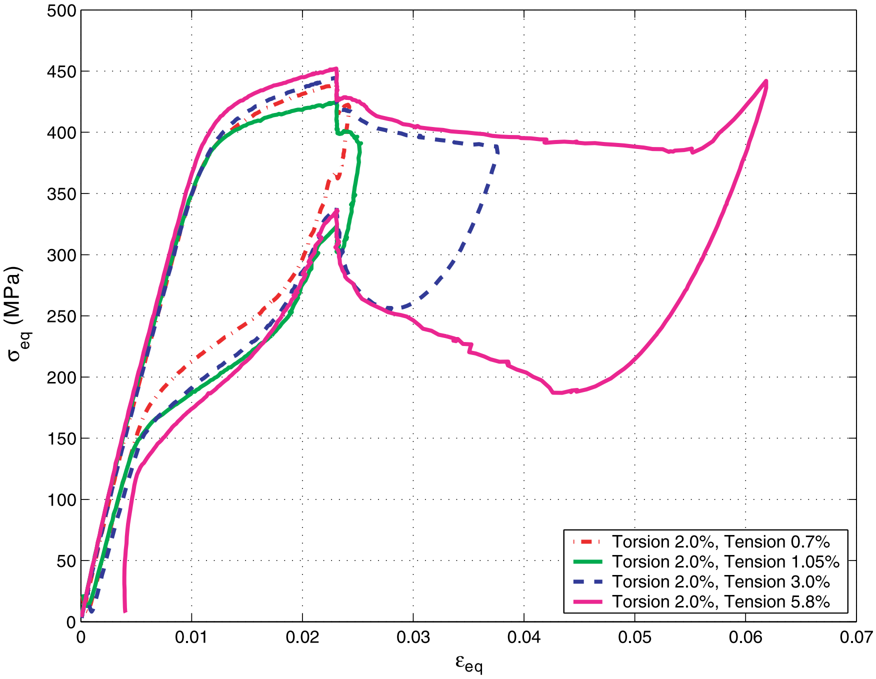

Fig. 14. Equivalent stress–strain plots in torsion (2%), followed by tension (0%, 0.7%, 1.05%, 3%, 5.8%) and reverse unloading (Type II).

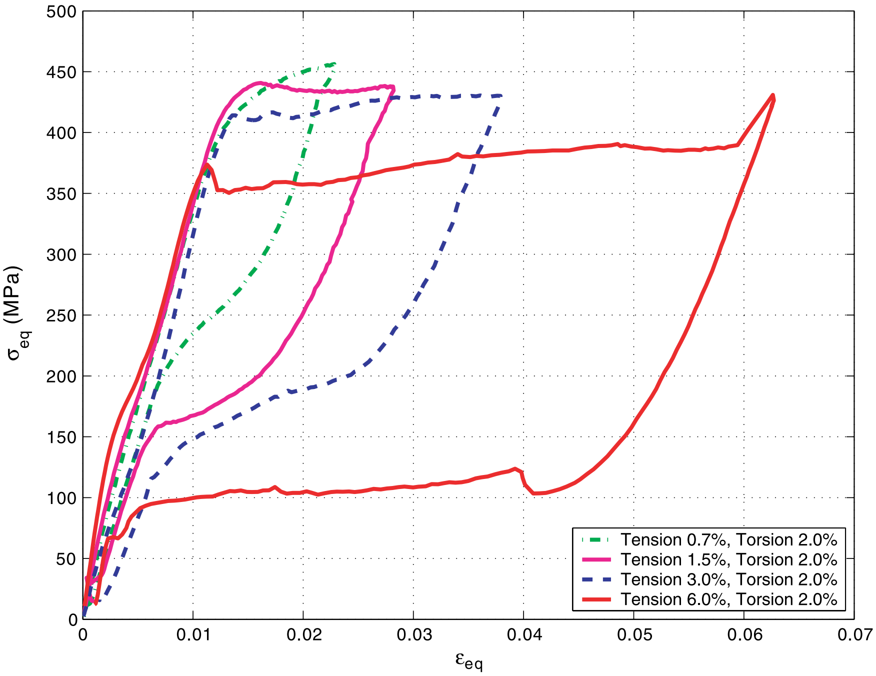

Fig. 15. Equivalent stress–strain plots in simultaneous tension (0%, 0.7%, 1.5%, 3%, 6%) and torsion (2%) with simultaneous unloading (Type III).

equivalent stress with decreasing applied equivalent strain. The micromechanical origin of this mechanical response is not presently understood. However, it does qualitatively indicate that the material has retained "memory" of its tensile transformation state.

A representative set of measurements in Fig. 12 illustrates the degree of repeatability for two particular Type I loading programs. As in the case of pure tension, X-ray diffractometry data on the unloaded specimens indicate the presence of residual martensite at small proportions (Fig. 13).

3.3. Torsion followed by tension (Type II)

In this case, torsion is applied corresponding to 2% strain, followed by tension up to 5.8% strain. Unloading is subsequently effected in the reverse order. Type II loading paths differ substantially from Type I paths, as readily seen in Fig. 14. Indeed, here the transformation plateau that follows the torsional loading occurs at monotonically decreasing stress levels. In addition, upon unloading, the "elastic" region is followed by reverse transformation along a plateau at monotonically increasing stress levels up to the point that corresponds to the end of the tensile unloading. Again, the material appears to exhibit memory of the transition from proportional to non-proportional loading.

3.4. Simultaneous tension–torsion (Type III)

The results of simultaneous proportional tension–torsion at up to 6.0% tensile strains and at 2.0% shear are depicted in Fig. 15. All loading paths produce curves which are qualitatively similar to those obtained under pure tension or torsion. In particular, smooth loading and unloading transformation plateaus are obtained at approximately constant stresses. This observation appears to support the conjecture that sharp changes in the stresses during non-proportional loading are

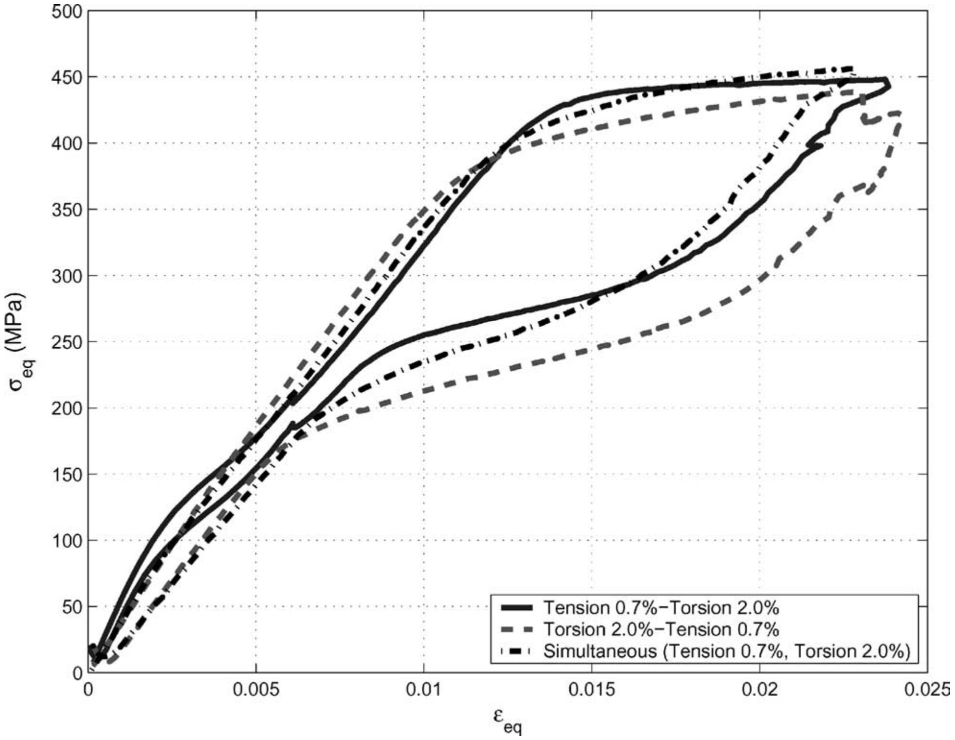

Fig. 16. Comparison of equivalent stress and strain behavior between loading paths at peak strains of 0.7% in tension and 2.0% in torsion.

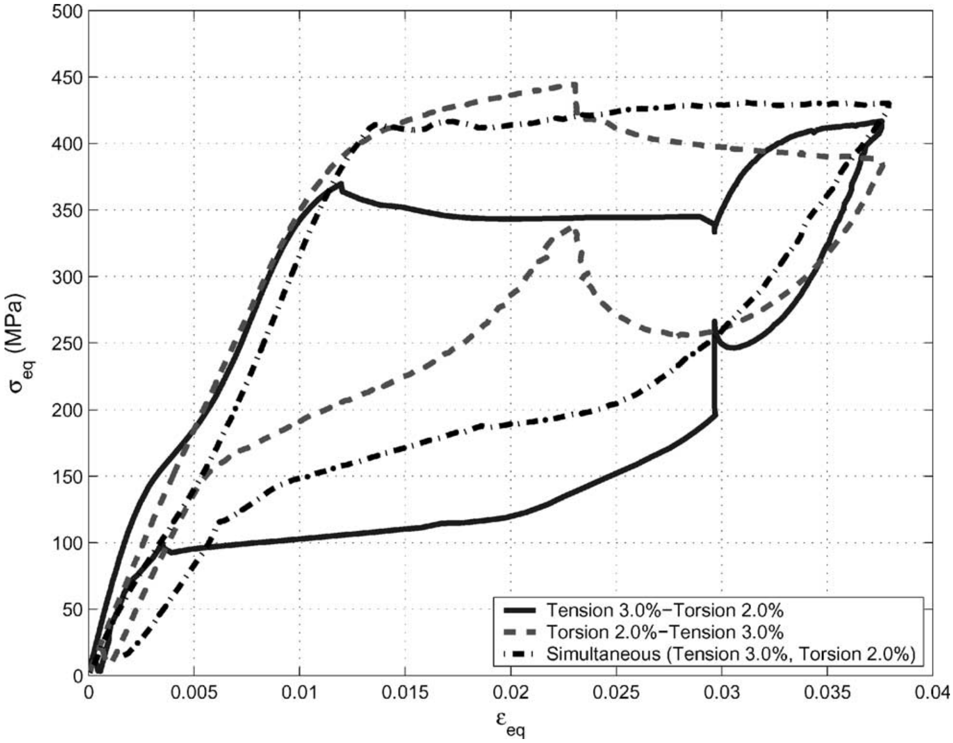

Fig. 17. Comparison of equivalent stress and strain behavior between loading paths at peak strains of 3.0% in tension and 2.0% in torsion.

effected by the generation of new sets of martensitic variants, while existing variants lead to higher stresses due to their energetic incompatibility with the current loading state. Additionally, it is observed that both the forward and reverse transformation stresses decrease with increasing proportion of the tensile loading, as expected.

3.5. Comparison of results from various loading path types

Figs. 16–18 compare Types I–III loading paths for various maximum tensile strains and at constant maximum shearing strain of 2%. At low tensile strain levels (Fig. 16), the loading paths are quite similar, although a small deviation is evident for the case of torsion followed by tensile loading. This apparent path-independence is not surprising considering the low level of applied tensile strain. At moderate tensile strains (Fig. 17), Type I and Type II loading generates widely differing non-smooth stress–strain curves, owing to the sharp transitions in variant formation at the transformation plateau. At a high tensile strain level (Fig. 18), the Types II and III paths yield remarkably similar curves, which can be explained by the predominantly proportional nature of both paths during the transformation process.

4. Analysis of results

The main features of the mechanical response of the tested polycrystalline Nitinol alloy are summarized and discussed in this section. In addition, the experimental results are reproduced using a proposed constitutive model for superelasticity.

4.1. Qualitative features

The experiments confirm that Nitinol produces essentially perfect stress–strain loops under cyclic

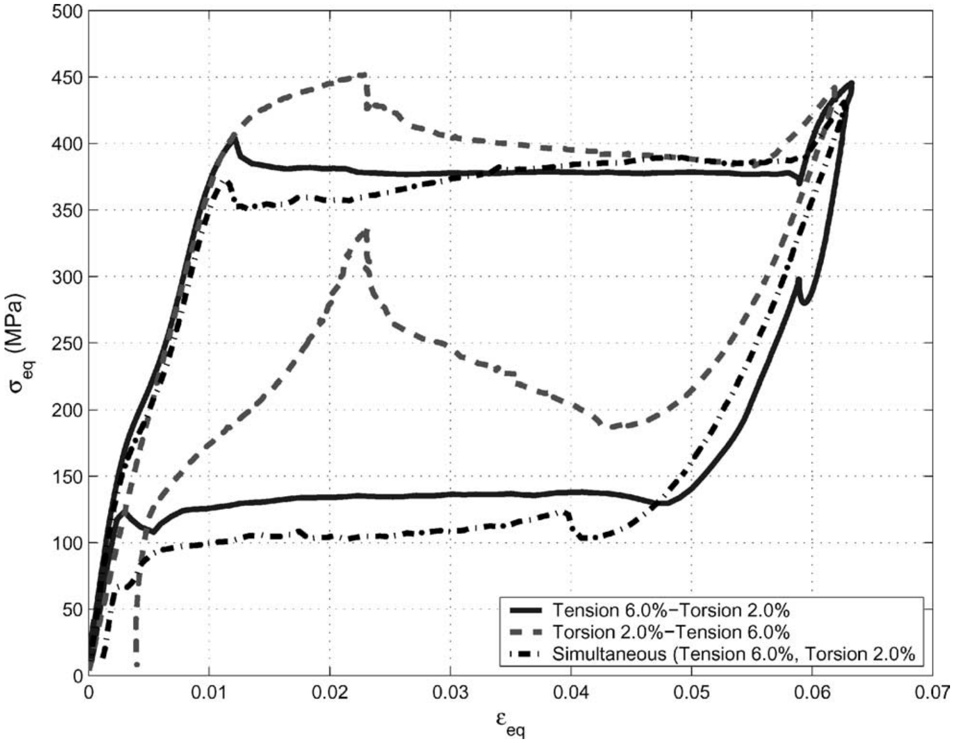

Fig. 18. Comparison of equivalent stress and strain behavior between loading paths at peak strains of 6.0% in tension and 2.0% in torsion.

loading in both tension and torsion. They also demonstrate that the development of a load-dependent microstructure is responsible for the non-smooth stress–strain curves under non-proportional loading of Types I and II. In addition, the alloy appears to exhibit memory of its forward transformation history throughout the loading process, as illustrated by the reverse transformation paths followed in the non-proportional loading cases.

Another important feature observed in the experiments is that the forward transformations in tension and torsion follow markedly different paths. In particular, and contrary to the case of initial yielding in metals, the transformation stress in torsion is consistently higher than in tension. In order to investigate further the different deformation mechanisms in tension and torsion, electropolished specimens were loaded according to the Types I and II protocol. During Type I loading, Lüders band formation was observed as soon as the tensile stress reached the plateau value of approximately 400 MPa at 1% tensile strain, as shown in Fig. 6(a) (see also (Shaw and Kyriakides, 1998)); the bands remained visible during the torsion cycle, where the tensile strain is held fixed. However, no Lüders bands were observed during Type II loading. It is conjectured that Lüders band formation during the tensile cycle facilitates the deformation, consistent with the higher stresses in torsion, where such bands do not appear to form, at least up to 2% shear strain. This is also supported by the simultaneous loading tests (Type III), where the plateau stress decreases with increasing tensile strain (Fig. 6(c)). These observations are consistent with the so-called ''yield drop'' in Nitinol (Eucken and Duerig, 1989). Another interesting qualitative characteristic of the stress–strain curves is that in the case of tension, there is a significant reduction in the elastic modulus at very low strains (approximately 0.3%), shown in Fig. 7, which may be attributed to the presence of the so-

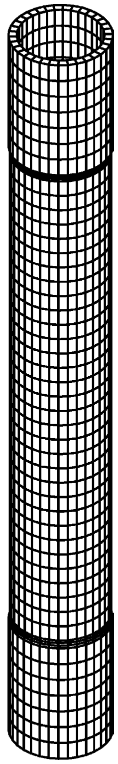

Fig. 19. Finite element mesh of the thin tubular specimen used in the numerical simulations.

called R-phase (Ling and Karlow, 1981). Interestingly, the torsion experiments show no such reduction in modulus (Fig. 9).

4.2. Constitutive modeling

The tension–torsion experiments described in Sections 2 and 3 were simulated by a finite element analysis using a three-dimensional superelasticity model in finite deformations. This is based on a thermomechanical single-crystal model by Siredey et al. (1999). The model predicts phase transformation potentially involving all 24 habit plane martensitic variants. Here, the equilibrium state of the austenitic matrix and the martensitic variants is determined by admitting a Helmholtz free energy

$$\Psi(\mathbf{E},\xi_\alpha)=\frac{1}{2}(\mathbf{E}-\mathbf{E}^{\mathrm{t}})\cdot\mathbb{C}(\mathbf{E}-\mathbf{E}^{\mathrm{t}})+\left(\sum_{\alpha=1}^{24}\xi_\alpha\right)B\theta \tag{1}$$

and stipulating that forward or reverse transformation occurs when the thermodynamic force associated with the volume fraction ξ_α ($\geqslant 0$) of each martensitic variant reaches a critical value. Notice that in Eq. (1), $\mathbf{E}$ denotes the Lagrangian strain tensor, $\mathbb{C}$ the (isotropic) fourth-order elasticity tensor, B the coefficient of chemical energy, and θ the relative temperature. Also, $\mathbf{E}^{\mathrm{t}}$ denotes the total Lagrangian transformation strain, expressed as

$$\mathbf{E}^{\mathrm{t}}=\sum_{\alpha=1}^{24}\xi_\alpha\mathbf{E}_\alpha^{\mathrm{t}} \tag{2}$$

in terms of the habit plane transformation variant strains $\mathbf{E}_\alpha^{\mathrm{t}}$. This habit plane-based model is preferable to lattice correspondence deformation models, because the latter assume that the parent phase transforms into martensitic variants without first forming a plate containing two twin-related martensite crystals, see (Gall et al., 1999). The habit plane transformation variant strain $\mathbf{E}_\alpha^{\mathrm{t}}$ for NiTi can be represented by the habit plane unit normal vector $\mathbf{n}_\alpha$, the displacement direction unit vector $\mathbf{m}_\alpha$, and the displacement magnitude g, in the form

$$\mathbf{E}_\alpha^{\mathrm{t}}=\frac{1}{2}g(\mathbf{m}_\alpha\otimes\mathbf{n}_\alpha+\mathbf{n}_\alpha\otimes\mathbf{m}_\alpha+g\mathbf{n}_\alpha\otimes\mathbf{n}_\alpha). \tag{3}$$

In the case of Nitinol single crystals, the base crystallographic vector parameters $\mathbf{n}$ and $\mathbf{m}$ have coordinates

$$\begin{aligned}(\mathbf{n})&=(-0.88888,0.21523,0.40443)^{\mathrm{T}},\\(\mathbf{m})&=(0.43448,0.75743,0.48737)^{\mathrm{T}},\end{aligned} \tag{4}$$

relative to the austenite lattice, while $g=0.13078$ (Buchheit and Wert, 1994). All twenty-four vector pairs $(\mathbf{n}_\alpha,\mathbf{m}_\alpha)$ are generated from (4) by appropriate rotations and reflections.

Material orientation (texture) has a profound effect on the mechanical response of the Nitinol tubes. Following the work of Gall and Sehitoglu (1999) and Gall et al. (1999), it is assumed that $\langle 1\,1\,1\rangle$ $\{1\,1\,0\}$-type sheet texture is "wrapped" around the cylindrical surface, such that the $\langle 1\,1\,1\rangle$ austenite lattice direction is aligned with the longitudinal axis of the tube. This type of texture is typically produced during cold-drawing along the

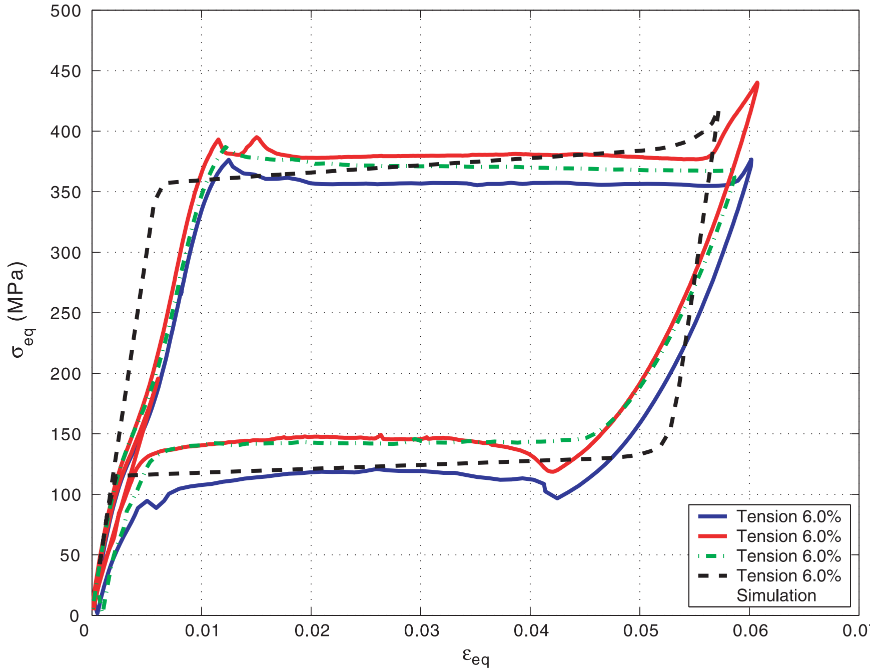

Fig. 20. Comparison of equivalent stress and strain plots between experiments and numerical simulation for uniaxial loading.

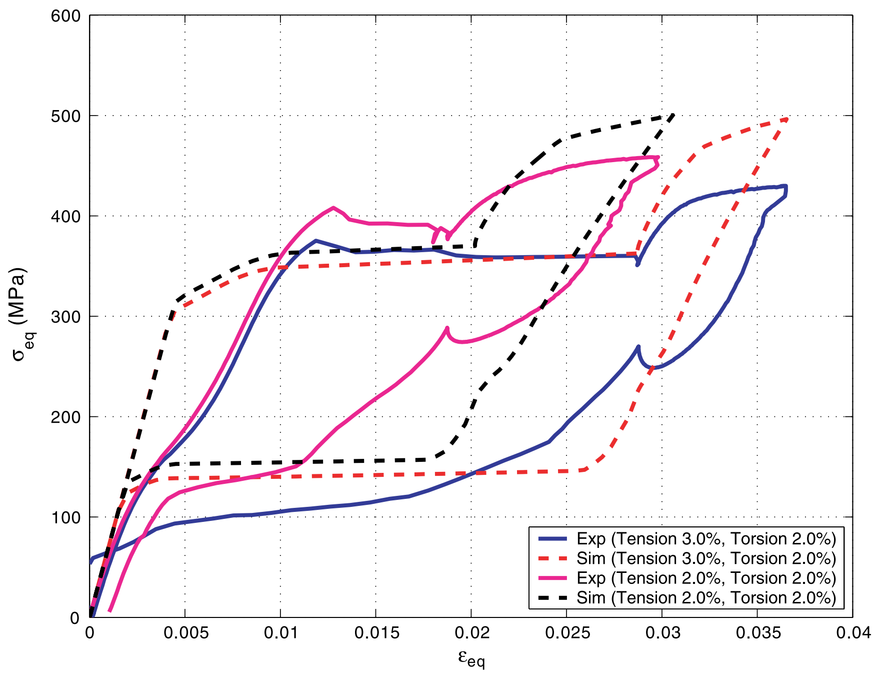

Fig. 21. Comparison of equivalent stress and strain plots between experiments and numerical simulation for Type I loading path.

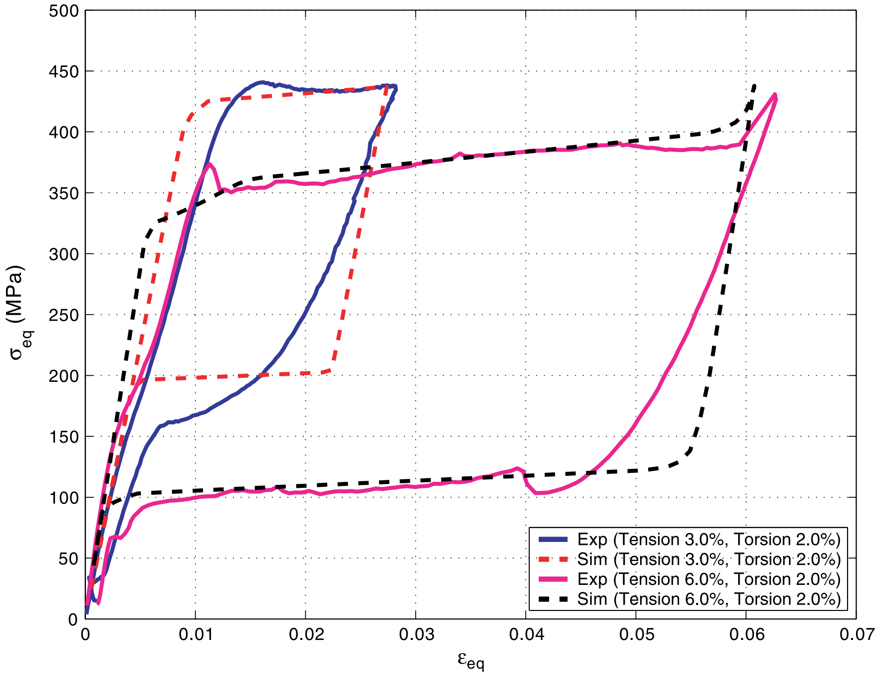

Fig. 22. Comparison of equivalent stress and strain plots between experiments and numerical simulation for Type III loading path.

longitudinal axis. The sheet texture assumption is also supported by the X-ray diffraction analysis (Fig. 3), in which B2 (1 1 0) phase is dominant. In real materials, a statistical variation from the texture within a deviation (wobble) is present, depending on the manufacturing process and geometric properties of the material. However, in this simulation, only the idealized texture effect has been considered in generating a polycrystal approximation.

A novel computational method for solving the constitutive equations associated with the above model is discussed in a companion paper (Jung et al., 2002). The finite element mesh of the specimen used in the experiments is shown in Fig. 19. The model predicts reasonably well the stress response in both tension and torsion, as illustrated in Figs. 20–22. Notice that the presence of R-phase is not included in the model, which results in a deviation of the numerically computed linearly elastic loading curve from the corresponding experimental one. Also, notice that the ear-shaped curve produced in the torsional loading/unloading stage is reproduced by the model, due to the latter's inclusion of different martensitic variants that can nucleate under non-proportional, non-simultaneous tensile and torsional loading shown in Fig. 21. This feature, which is clearly exhibited in the experiments and replicated in the numerical simulation, has been difficult to capture using phenomenological constitutive models.

5. Conclusions

Tension–torsion experiments on thin-walled superelastic Nitinol tubes have demonstrated a rich mechanical behavior involving significantly different characteristics in each of the two loading axes. The observed behavior provides important insights to the stress-induced phase transformation under multiaxial loading commonly encountered in a wide array of engineering applications involving superelastic materials. The experiments and simulations suggest that the characterization and modeling of the microstructure is of paramount importance in understanding the phenomenology of shape-memory alloys.

Acknowledgements

This work was supported by the National Science Foundation under contract Nr. CMS-9800006 with the University of California, Berkeley. Special thanks are due to Dr. Thomas W. Duerig of Nitinol Devices & Components (Fremont, California) for supplying the Nitinol tubing and for many helpful discussions. V.I. also wishes to thank Professor Giuseppe Palombarini (Instituto di Metallurgia, Università di Bologna, Italy) for his support. Finally, the authors would like to thank R.K. Nalla for performing the diffraction analysis at the Stanford Synchrotron Radiation Laboratory.

References

Buchheit, T.E., Wert, J.A., 1994. Modeling the effects of stress state and crystal orientation on the stress-induced transformation of NiTi single crystals. Metall. Mater. Trans. A 25, 2383–2389.

Buehler, W.J., Wiley, R.C., 1965. Nickel-based alloys. Technical report, US Patent 3174851.

Duerig, T.W., Tolomeo, D.E., Wholey, M., 2000. An overview of superelastic stent design. Minimally Invasive Ther. Allied Tech. 9, 235–246.

Eucken, S., Duerig, T.W., 1989. The effects of pseudoelastic prestraining on the tensile behaviour and 2-way shape memory effect in aged Ni–Ti. Acta Metall. 37, 2245–2252.

Gall, K., Sehitoglu, H., 1999. The role of texture in tension–compression asymmetry in polycrystalline NiTi. Int. J. Plast. 15, 69–92.

Gall, K., Sehitoglu, H., Chumlyakov, Y.I., Kireeva, I.V., 1999. Tension–compression asymmetry of the stress–strain response in aged single crystal and polycrystalline NiTi. Acta Mater. 47 (4), 1203–1217.

Helm, D., Haupt, P., 2001. Active materials: behavior and mechanics. In: C.S. Lynch, (Ed.), Smart Structures and Materials. Bellingham, SPIE, 4333, pp. 302–313.

Jung, Y., Papadopoulos, P., Ritchie, R.O., 2002. Constitutive modeling and numerical simulation of multivariant phase transformation in superelastic alloys. Int. J. Numer. Methods Engin., submitted.

Lim, T.J., McDowell, D.L., 1999. Mechanical behavior of an Ni–Ti shape memory alloy under axial-torsional proportional and nonproportional loading. ASME J. Eng. Mater. Tech. 121, 9–18.

Lim, T.J., McDowell, D.L., 1995. Path dependence of shape memory alloys during cyclic loading. J. Intell. Mater. Sys. Struct. 6, 817–830.

Ling, H.C., Karlow, R., 1981. Stress-induced shape changes and shape memory in the R and martensite transformations in equiatomic NiTi. Metall. Trans. A 12A, 2101–2111.

Miyazaki, S., Otsuka, K., Wayman, C.M., 1989. The shape memory mechanism associated with the martensitic transformation in Ti–Ni alloys. 1. Self-accommodation. Acta Metall. 37, 1873–1890.

Shaw, J.A., Kyriakides, S., 1998. Initiation and propagation of localized deformation in elasto-plastic strips under uniaxial tension. Int. J. Plast. 13, 837–871.

Siredey, N., Patoor, E., Berveiller, M., Eberhardt, A., 1999. Constitutive equations for polycrystalline thermoelastic shape memory alloys. Part I. Intragranular interactions and behavior of the grain. Int. J. Solids Struct. 36, 4289–4315.

Sun, Q.P., Hwang, K.C., 1993. Micromechanics modelling for the constitutive behavior of polycrystalline shape memory alloys. I. Derivation of general relations. J. Mech. Phys. Sol. 41, 1–17.

Wayman, C.M., Duerig, T.W., 1990. An introduction to martensite and shape memory. In: Duerig, T.W., Melton, K.N., Stökel, D., Wayman, C.M. (Eds.), Engineering Aspects of Shape Memory Alloys. Butterworth-Heinemann, London, pp. 3–20.